Models of collective cell spreading with variable cell aspect ratio: A motivation for degenerate diffusion models

Matthew J. Simpson,[1,2] Ruth E. Baker,[3] and Scott W. McCue[1]

[1]*Mathematical Sciences, Queensland University of Technology, Brisbane, Australia*

[2]*Tissue Repair and Regeneration Program, Institute of Health and Biomedical Innovation (IHBI), Queensland University of Technology, Brisbane, Australia*

[3]*Centre for Mathematical Biology, Mathematical Institute, University of Oxford, 24-29 St Giles', Oxford, OX1 3PN, United Kingdom*

(Received 21 August 2010; revised manuscript received 26 October 2010; published 2 February 2011)

Continuum diffusion models are often used to represent the collective motion of cell populations. Most previous studies have simply used linear diffusion to represent collective cell spreading, while others found that degenerate nonlinear diffusion provides a better match to experimental cell density profiles. In the cell modeling literature there is no guidance available with regard to which approach is more appropriate for representing the spreading of cell populations. Furthermore, there is no knowledge of particular experimental measurements that can be made to distinguish between situations where these two models are appropriate. Here we provide a link between individual-based and continuum models using a multiscale approach in which we analyze the collective motion of a population of interacting agents in a generalized lattice-based exclusion process. For round agents that occupy a single lattice site, we find that the relevant continuum description of the system is a linear diffusion equation, whereas for elongated rod-shaped agents that occupy L adjacent lattice sites we find that the relevant continuum description is connected to the porous media equation (PME). The exponent in the nonlinear diffusivity function is related to the aspect ratio of the agents. Our work provides a physical connection between modeling collective cell spreading and the use of either the linear diffusion equation or the PME to represent cell density profiles. Results suggest that when using continuum models to represent cell population spreading, we should take care to account for variations in the cell aspect ratio because different aspect ratios lead to different continuum models.

DOI: 10.1103/PhysRevE.83.021901 PACS number(s): 87.17.Aa, 87.10.Rt, 87.17.Jj

I. INTRODUCTION

A. Biological motivation

Continuum models of collective cell spreading based on linear diffusion, which give rise to cell density descriptions of the form

$$\frac{\partial C}{\partial t} = D_0 \nabla^2 C, \tag{1}$$

are routinely used to model the collective movement of cell populations [1–6]. Several authors have also suggested that the traditional linear diffusion mechanism can be generalized to a nonlinear diffusion model

$$\frac{\partial C}{\partial t} = D_0 \nabla \cdot [D(C) \nabla C] \tag{2}$$

with $D(C) = C^n$ and $n > 0$ [1,3,5,7]. This degenerate nonlinear diffusion equation is known as the porous media equation (PME) [8,9], which is degenerate in the sense that $D(0) = 0$. In Eqs. (1)–(2) D_0 is the free cell diffusivity and $D(C)$ is the nonlinear diffusivity function.

One of the main arguments supporting the use of the PME to model the spreading of cell populations is that the solution of the PME can have distinct boundaries, called interfaces, beyond which the population density is zero [8–10]. These sharp-fronted solutions are thought to represent sharp-fronted cell density profiles [1]. Other justifications for using the PME borrow from arguments that arose in the ecology and animal dispersal literature [11–13]. In particular, Murray discusses how the PME can represent "population pressure" in biological systems [14].

Although many theoretical treatments of the PME are partly justified by their relevance to biological motility problems [7,10,15–18], the assumption that the evolution of a spreading cell population is governed by the PME has never been formally justified. Often the PME has been used in preference to the linear diffusion equation because of model calibration arguments. For example, Sherratt and Murray [3] modeled a set of wound closure experiments using two different continuum models. One model involved a linear diffusion motility mechanism, and the other involved a degenerate nonlinear diffusion motility mechanism, where the nonlinear diffusivity function was given by $D(C) = C^4$. The results presented in this previous work show that the solutions of the model incorporating degenerate nonlinear diffusion provided a better fit to the experimental data than the solutions of the model with a linear diffusion motility mechanism. Similarly, Sengers and coworkers [5] modeled a set of *in vitro* cell invasion assays describing two different skeletal cell types, including MG63 cells and human bone marrow stromal cells (HBMSCs). They collected detailed experimental data that described the evolution of cell density profiles, and the solution of a reaction-diffusion equation was fitted to the experimental data using a least-squares approach. Key results from the study by Sengers and coworkers are shown in Fig. 1, where detailed cell density data are compared with the solution of the reaction-diffusion model. These results show that the spreading of the HBMSC population was best described by a linear diffusion motility mechanism [Fig. 1(a)] whereas the spreading of the MG63 population was best described by a degenerate nonlinear diffusion motility mechanism with a nonlinear diffusivity function given by $D(C) = C$ [Fig. 1(b)].

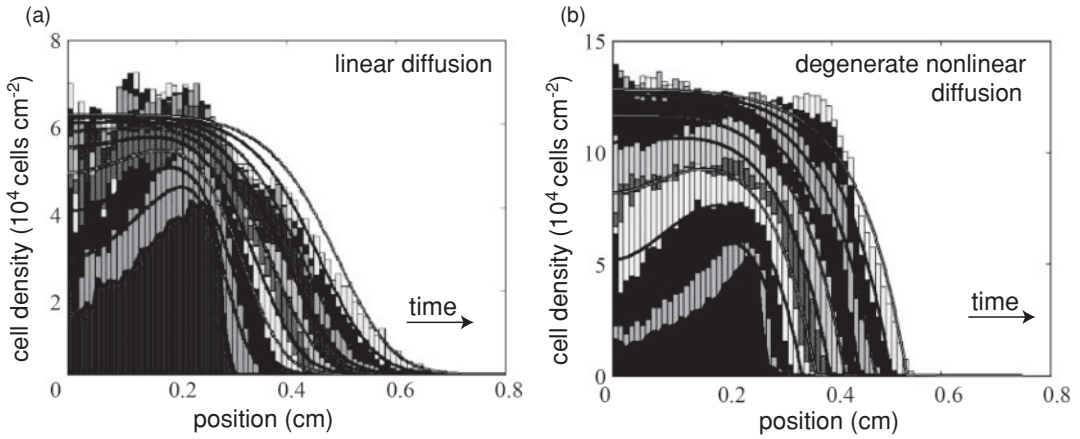

FIG. 1. (a) Experimental cell density profiles from an *in vitro* cell spreading assay using human skeletal HBMSC cells. Experimental cell density data (histograms) are matched with the solution of a continuum model (solid lines) with a linear diffusion mechanism. The numerical solutions of the continuum model are smooth fronted. (b) Experimental cell density profiles from an in vitro cell spreading assay using human skeletal MG63 cells. Experimental cell density data (histograms) are matched with the solution of a continuum model (solid lines) with a nonlinear degenerate diffusion mechanism with $D(C) = C$. The numerical solutions of the continuum model are sharp fronted. Full experimental and modeling details are available in Ref. [5]. Reprinted from J R Soc Interface (2007), Sengers BG, Please CP, and Oreffo ROC, Experimental characterization and computational modelling of two-dimensional cell spreading for skeletal regeneration, 4, 1107–1117 (2007) with permission from the Royal Society.

These previous observations raise several important questions:

(1) Why is the spreading of certain cell populations best described by a linear diffusion mechanism?

(2) Why is the spreading of certain cell populations best described by a PME model?

(3) When we apply the PME to represent collective cell spreading, how do we choose the exponent n in the nonlinear diffusivity function $D(C) = C^n$?

Currently there is no accepted mathematical or physical justification available to answer to any of these questions. Instead of relying on *ad hoc* arguments based on intuition or model calibration, here we take a different approach and show that the PME plays an important role in describing the spreading of cell populations when we consider the effects of varying the cell aspect ratio together with volume exclusion.

Having an understanding of how to choose the appropriate motility term in a partial differential equation (PDE) model to describe the spreading of cell populations has very broad and important implications. This is because continuum models of cell population spreading are routinely used in several applications including wound healing [1,2], developmental biology [6], and cancer biology [19]. If we choose to model the spreading of a cell population using a PDE, we must somehow choose the most appropriate motility term in the PDE. Making this choice is fraught with difficulties because many different motility mechanisms can be used to match experimental data via model calibration arguments [20]. Instead of relying on intuition or calibration, here we consider several discrete motility mechanisms and analyze their relationship with a PDE model by considering the continuum limit of the processes.

B. Connection with existing work

Recently we [21–24] and others [25–28] have used discrete interacting random walk models, called exclusion processes [29], to represent collective cell spreading. Exclusion processes are lattice-based random walk models in which each lattice site can be occupied by, at most, one agent. Simulations of exclusion process models provide us with microscopic data, and averages constructed using these microscopic data provide a macroscopic continuum description of the system that can be related to the solution of a PDE [22–25].

Previous applications of exclusion process models have considered each biological cell to be represented by a single agent that occupies a single lattice site. These existing models are appropriate for modeling "round" cells where the longitudinal and transverse length scales of the cell are approximately equal. This is true of our previous work [21–24] and the previous work of others [25–28]. Our new work is motivated by the fact that cells are not always round, but are often elongated or rod shaped, such as the population of cells shown in Fig. 2(a). In this case the cell length along the longitudinal axis is approximately four times the cell length along the transverse axis, giving an aspect ratio of $L = 4$. By developing new exclusion process-based models using elongated agents to represent elongated cells, the current work is a major extension of existing work, which was limited to the simplest possible case where $L = 1$ [22].

In Sec. II we develop exclusion process models relevant to populations of cells with different, fixed aspect ratios. These models are simulated on a square two-dimensional lattice with spacing Δ. Each site is indexed (i, j) where $i, j \in \mathbb{Z}^+$, and each site has position $(x, y) = (i\Delta, j\Delta)$. The length of the lattice is given by the x coordinate, $1 \leqslant x \leqslant x_{\max}$, and the vertical height of the lattice is given by the y coordinate, $1 \leqslant y \leqslant y_{\max}$. A population of interacting agents is considered in which each agent has an aspect ratio of L and occupies L (horizontally or vertically) adjacent lattice sites. For example, an agent that is parallel to the x axis with $L = 2$ might occupy sites (i, j) and $(i + 1, j)$. Alternatively, an agent that is parallel to the

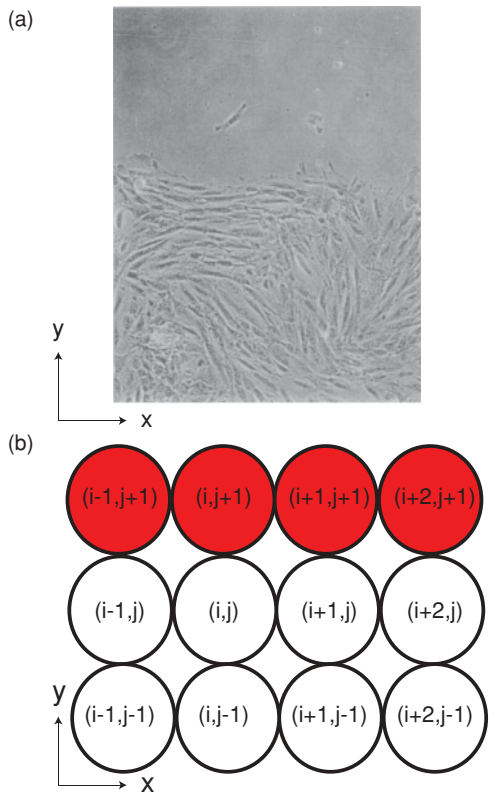

FIG. 2. (Color online) (a) An image from an *in vitro* wound-healing scratch assay showing a population of human peritoneal mesothelial cells. During the assay cells are motile and proliferative resulting in the leading edge of the population moving in the positive y direction. This image was taken about 10 hours after wounding, and full details of this experiment are described by Maini *et al.* [1,2]. The typical length scale of each cell is 10–20 μm. Reprinted from Appl. Math. Lett., Maini PK, McElwain DLS, and Leavesley D, Travelling waves in a wound healing assay, 17, 575–580 (2004) with permission from Elsevier. (b) A portion of a lattice partly occupied by a single red agent (gray) with $L = 4$ that is parallel to the x axis and occupies sites $(i-1, j+1)$, $(i, j+1)$, $(i+1, j+1)$, and $(i+2, j+1)$.

y axis with $L = 2$ might occupy sites (i, j) and $(i, j+1)$. By considering the continuum limit of these discrete models, we provide a novel motivation for the use of the PME to represent the spreading of cell populations. Our analysis also shows that the relevant continuum model simplifies to the linear diffusion equation when $L = 1$. Therefore, our work provides a connection between the use of linear diffusion and degenerate nonlinear diffusion models in this context. Further, our results suggest that the differences between these two models can arise due to differences in agent aspect ratio, and we conclude that measurements of the cell aspect ratio ought to be made to help distinguish between the use of the linear diffusion equation and the PME. In Sec. III we provide simulations and analysis of more complex systems with interacting subpopulations that are relevant to more complicated situations.

II. A POPULATION OF HORIZONTALLY ALIGNED AGENTS

A. Discrete simulations

To illustrate the influence of varying the aspect ratio of agents, we first consider the simplest system with a population of uniformly aligned agents, each with the same aspect ratio, L. In the first instance we consider the case where all agents are parallel to the x axis. For example, the red agent in Fig. 2(b) has $L = 4$ and occupies four adjacent lattice sites: $(i-1, j+1)$, $(i, j+1)$, $(i+1, j+1)$, and $(i+2, j+1)$. The motility of a population of N such agents is simulated as follows: During each time step of duration τ, N agents are selected independently at random, one at a time, and given the opportunity to move. This is called a random sequential update method [30]. When chosen, an agent attempts to move with probability $P_m \in [0,1]$. We interpret P_m as the probability that an agent will attempt to move a distance Δ in the time interval τ. For example, if the agent in Fig. 2(b) were to move in the positive x direction, at the end of the motility event sites $(i, j+1)$, $(i+1, j+1)$, $(i+2, j+1)$, and $(i+3, j+1)$ would be occupied, and site $(i-1, j+1)$ would be vacant. Similarly, if the agent in Fig. 2(b) were to move in the negative y direction, at the end of the motility event sites $(i-1, j)$, (i, j), $(i+1, j)$, and $(i+2, j)$ would be occupied, while sites $(i-1, j+1)$, $(i, j+1)$, $(i+1, j+1)$, and $(i+2, j+1)$ would be vacant. If, during the attempted motility event, any target site is occupied by any agent other than the agent attempting to move, then that motility event is aborted.

Using this mechanism with a population of horizontally aligned agents with $L = 4$, we conducted simulations on a lattice with $1 \leqslant x \leqslant 400$ and $1 \leqslant y \leqslant 20$. The central part of this lattice is shown in Fig. 3(a). Periodic boundary conditions were imposed at $y = 1$ and $y = 20$, and reflecting boundary conditions were imposed at $x = 1$ and $x = 400$. All lattice sites between $181 \leqslant x \leqslant 220$ were initially occupied so that the initial distribution of agents was composed of 10 columns of adjacent nonoverlapping agents, each with $L = 4$. The system was allowed to evolve, and we observe the spreading of the population in Figs. 3(a)–3(c) at $t = 0, 100, 300$, respectively. To complement this single microscopic realization, we also generated averaged agent density data in Fig. 3(d) for the same problem at $t = 0, 100, 300$.

To generate these data, we construct an appropriate measure of the averaged agent density profile using the following argument. If $C^m(i, j)$ is the occupancy of site (i, j) during the mth realization, then for M realizations starting from the same initial condition, we can estimate the occupancy of any site within a particular column by constructing a double average across the height of the column $y_{\max}$, and over M identically prepared realizations, given by

$$\langle C(x,t)\rangle = \frac{1}{y_{\max} M} \sum_{m=1}^{M} \sum_{y=1}^{y_{\max}} C^m(i,j). \tag{3}$$

Our previous work has shown that when the initial occupancy of all sites within every column of the lattice is constant, and we perform simulations with periodic boundary conditions on the horizontal boundaries, then the dynamics of the system

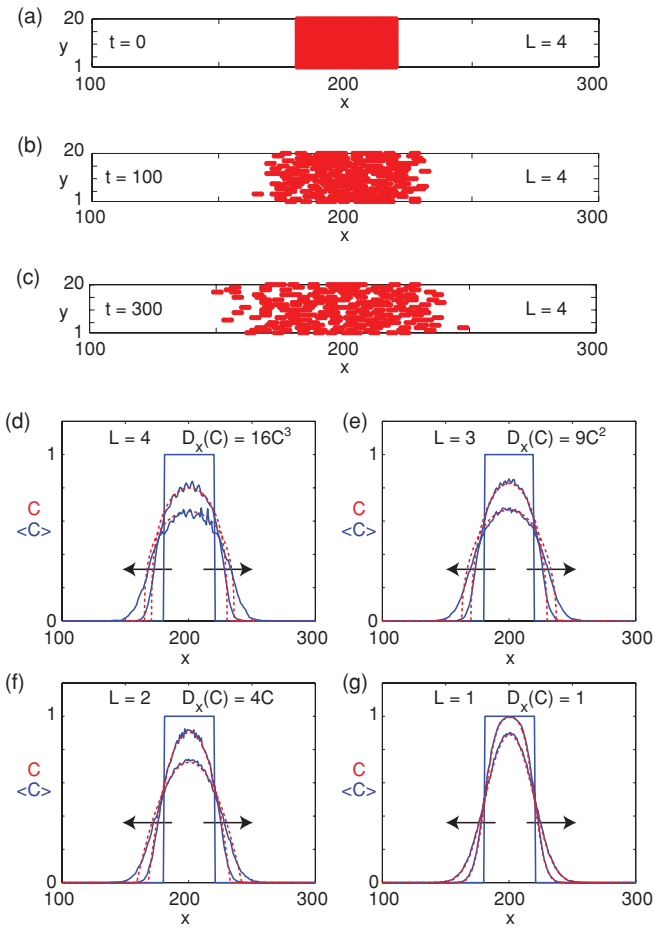

FIG. 3. (Color online) (a) Simulations start with all sites occupied where $181 \leqslant x \leqslant 220$ so that the initial population is composed of 10 adjacent columns of nonoverlapping horizontally aligned agents each with $L = 4$. (b)–(c) Simulation results are given at $t = 100,300$ for $P_m = \Delta = \tau = 1$. Results in (d)–(g) show averaged agent density data for a series of simulations, similar to those shown in (a)–(c), for $L = 4,3,2,1$, respectively. In (d)–(g) we consider 10, 13, 20, 40 adjacent columns of nonoverlapping horizontally aligned agents with $L = 4,3,2,1$ so that all sites with $181 \leqslant x \leqslant 220$, $181 \leqslant x \leqslant 219$, $181 \leqslant x \leqslant 220$, $181 \leqslant x \leqslant 220$ are initially occupied. In each case, the column density of agents averaged over $M = 100$ identically prepared simulations, $\langle C(x,t)\rangle$, is shown in blue (solid) at $t = 0,100,300$. These simulation profiles are compared with the solution of Eq. (6) shown in red (dotted) with the arrows showing the direction of increasing time. The solution of Eq. (6) is obtained numerically using the method described in the main text with $\delta x = 0.25$, $\delta t = 0.1$, and $\epsilon = 1 \times 10^{-6}$.

reduces to a one-dimensional problem where we need only consider the x component of the density information [22–24]. Under these conditions the double average given by Eq. (3) is a useful measure of the x component of the agent density [22–24]. Using Eq. (3) with $M = 100$ identically prepared realizations, the density data in Fig. 3(d) show how the population spreads away from the initial closely packed distribution. For comparison purposes, we simulated three further problems similar to the results in Figs. 3(a)–3(d), except that the agents have different aspect ratios $L = 3,2,1$. Details of these these additional simulations are given in Figs. 3(e)–3(g).

Comparing the discrete density profiles in Figs. 3(d)–3(g) we see the importance of accounting for differences in agent aspect ratio; the evolution of the density profiles is very different as L is varied. For example, we see that the agent density near $x = 200$ decreases faster as L increases. This observation is intuitively reasonable. Consider a single agent with $L = 1$ located at (i,j). If this agent moves in the positive x direction, the density of sites (i,j) and $(i+1,j)$ are altered. In comparison, consider the movement of an agent with $L = 4$. If the agent occupies sites $(i-3,j)$, $(i-2,j)$, $(i-1,j)$, and (i,j), and the agent moves in the positive x direction, this event alters the density at site $(i+1,j)$ as well as the distant site $(i-3,j)$. This argument illustrates why the density profiles in Figs. 3(d)–3(g) spread faster as L increases: The movements of larger agents affect the population density over a wider region of the lattice relative to the same event acting on a population of smaller agents.

At this stage we would like to point out a common difficulty regarding the interpretation of experimental measurements. The agent density profiles in Figs. 3(d)–3(g) represent spreading cell density profiles. In the absence of any detailed knowledge about the underlying discrete motility mechanism, a standard approach to using a mathematical model to represent this kind of data would be to fit (what is thought to be) the solution of an appropriate model to these density data [3,5]. Given that each density profile in Figs. 3(d)–3(g) remains symmetric relative to the initial distribution, it would be reasonable to fit the solution of a linear diffusion equation to these data using a least-squares approach [5,31]. As we have already observed, each of the density profiles in Figs. 3(d)–3(g) is quite different, and this model calibration procedure would lead us to arrive at different estimates of the free cell diffusivity, D_0, for each value of L. Instead of this *ad hoc* model calibration procedure, in Sec. II C we will show that different values of L are related to different diffusion mechanisms with different nonlinear diffusivity functions $D(C)$; however, the free cell diffusivity, D_0, for each result in Figs. 3(d)–3(g) is the same.

B. Convergence behavior of the agent density profiles

It is useful to investigate how density data obtained from Eq. (3) converge to a reliable estimate as either the vertical height of the lattice, $y_{\max}$, or the number of identically prepared realizations, M, increases. In the simplest possible case, we could repeat any of the simulations in Figs. 3(d)–3(g) by setting $y_{\max} = 1$ and performing $M = 1$ realization only. Under these conditions the density profiles given by Eq. (3) would contain large fluctuations, and it would be impossible to deduce anything meaningful by inspecting the resulting density profile. The reason for this is that there are insufficient numbers of agents on the lattice to draw conclusions about the mean agent density profile. There are two simple ways to overcome this problem. Either (i) we can increase the vertical height of the lattice $y_{\max}$ or (ii) we can increase the number of identically prepared realizations M. Both these approaches ensure that the average density profiles obtained using Eq. (3) are constructed using very large numbers of agents resulting in a reliable approximation to the agent density profile. Since we

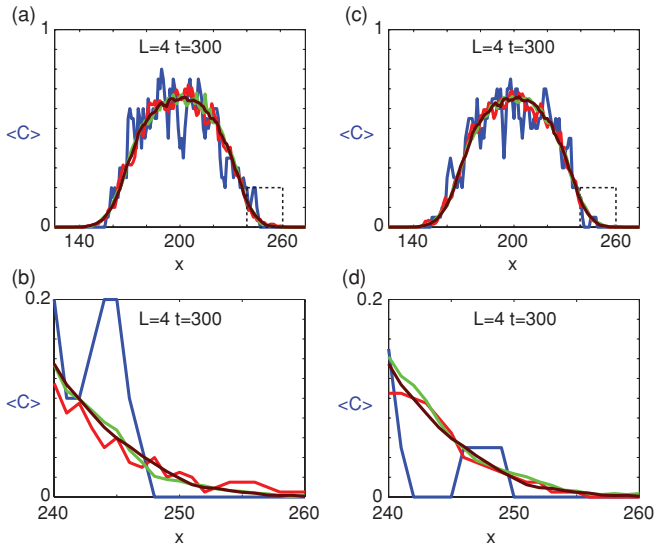

FIG. 4. (Color online) Convergence of the column averaged agent density profiles obtained using Eq. (3) for a suite of simulations that start with all sites occupied where $181 \leqslant x \leqslant 220$ so that the initial population is composed of 10 adjacent columns of nonoverlapping horizontally aligned agents each with $L = 4$ [equivalent to the results in Fig. 3(d)]. All simulations are performed until $t = 300$ for $P_m = \Delta = \tau = 1$. Results in (a) correspond to a lattice with a vertical height $y_{\max} = 20$. Four density profiles are shown where averages are constructed with $M = 1,10,100,200$ shown in blue, red, green, and brown (dark gray, light gray, lighter gray, darker gray), respectively. The details of the column averaged density profile in the tail region between $240 \leqslant x \leqslant 260$ is shown in (b). Similar results in (c) correspond to averages generated using $M = 10$ identically prepared realizations. Four density profiles are shown where averages are constructed on lattices with different vertical heights $y_{\max} = 2,20,200,400$ shown in blue, red, green, and brown (dark gray, light gray, lighter gray, darker gray), respectively. The details of the column averaged density profile in the tail region between $240 \leqslant x \leqslant 260$ is shown in (d).

are performing simulations we are free to choose $y_{\max}$ and/or M to be as large as we wish, meaning that we can generate very reliable density profiles.

To demonstrate how the density profiles described by Eq. (3) converge as either $y_{\max}$ or M increases, we provide additional simulation data in Fig. 4. In Fig. 4(a) we repeat the simulation shown in Fig. 3(d) and present density information at $t = 300$. This density profile is obtained using a lattice with $y_{\max} = 20$, and we show agent density data obtained from Eq. (3) using $M = 1,10,100$ and $M = 200$ identically prepared realizations. The results in Fig. 4(a) indicate that the density profile obtained with $M = 1$ contains large fluctuations, while the results with $M = 10,100,200$ show rapidly smoothing profiles where the fluctuations decrease quickly as M increases. For low values of M, the density data are unreliable. This is particularly true near the leading edges of the profile since there are a small number of agents in this region. To emphasize the rapid convergence of the density data as M increases, we also show details of the density profile at the leading edge where $240 \leqslant x \leqslant 260$ in Fig. 4(b). In this leading-edge region we observe rapid convergence of the density profile even though the number of agents present in this location in any particular realization of the discrete algorithm is relatively small. The key to obtaining reliable density information at all locations on the lattice is to consider a sufficiently large number of identically prepared realizations so that the fluctuations about the mean profile become sufficiently small.

Instead of considering a fixed value of $y_{\max}$ and increasing M as we did in Fig. 4(a)–4(b), we could also consider fixing a value of M and considering the density profiles as $y_{\max}$ increases. Results in Fig. 4(c) show equivalent density profiles that were given in Fig. 4(a) except here we consider $M = 10$ and we increase the vertical height of the lattice from $y_{\max} = 2,20,200$ to $y_{\max} = 400$. As we vary the vertical height of the lattice, we alter our initial condition so that all parts of the lattice with $181 \leqslant x \leqslant 220$ are occupied by 10 adjacent columns of nonoverlapping agents with $L = 4$. This change in initial condition alters the number of agents in each simulation. For example, with $y_{\max} = 2,20,200,400$ our simulations contain 20,200,2000 and 4000 agents, respectively. Similar to the results in Fig. 4(a), we observe that the density profiles with small $y_{\max}$ display large fluctuations. However, we observe rapid convergence of the density profiles as $y_{\max}$ is increased. This means that we can reliably estimate the average density profile at any location across the lattice. In Fig. 4(d) we zoom in on the region where $240 \leqslant x \leqslant 260$ showing that the density data at the leading edge also converge to a reliable approximation of the agent density profile.

In summary, when we consider simulations where the initial occupancy of all sites within each column of the lattice is constant, and we impose periodic boundary conditions on the horizontal boundaries of the lattice, the density profiles obtained using Eq. (3) with sufficiently large $y_{\max}$ and/or sufficiently large M are reliable at all locations across the lattice.

C. A continuum model

To connect the discrete mechanism with a continuum model we average the occupancy of site (i,j) over many statistically identical realizations to obtain $\langle C_{i,j}\rangle \in [0,1]$ [22–24]. After averaging, we form a discrete conservation statement describing $\delta\langle C_{i,j}\rangle$, which is the change in average occupancy of site (i,j) during the time interval from t to $t+\tau$. For a system with a population of horizontally aligned agents, each with the same aspect ratio L, the discrete conservation statement can be written as

$$\begin{aligned}\delta\langle C_{i,j}\rangle = {} & \frac{P_m}{4}\left(\prod_{s=1}^{L}\langle C_{i-s,j}\rangle + \prod_{s=1}^{L}\langle C_{i+s,j}\rangle\right)(1-\langle C_{i,j}\rangle) \\ & + \frac{P_m}{4}\sum_{m=1-L}^{0}\left[\prod_{s=m}^{m+L-1}\langle C_{i-s,j+1}\rangle(1-\langle C_{i-s,j}\rangle)\right] \\ & + \frac{P_m}{4}\sum_{m=1-L}^{0}\left[\prod_{s=m}^{m+L-1}\langle C_{i-s,j-1}\rangle(1-\langle C_{i-s,j}\rangle)\right] \\ & - \frac{P_m}{4}\left(\prod_{s=0}^{L-1}\langle C_{i-s,j}\rangle\right)(1-\langle C_{i-L,j}\rangle)\end{aligned}$$

$$- \frac{P_m}{4}\left(\prod_{s=0}^{L-1}\langle C_{i+s,j}\rangle\right)(1-\langle C_{i+L,j}\rangle) - \frac{P_m}{4}\sum_{m=1-L}^{0}\left[\prod_{s=m}^{m+L-1}\langle C_{i-s,j}\rangle(1-\langle C_{i-s,j-1}\rangle)\right] - \frac{P_m}{4}\sum_{m=1-L}^{0}\left[\prod_{s=m}^{m+L-1}\langle C_{i-s,j}\rangle(1-\langle C_{i-s,j+1}\rangle)\right]. \quad (4)$$

Positive terms on the right of Eq. (4) represent motility events that increase the occupancy of site (i,j), while negative terms on the right of Eq. (4) represent motility events that decrease the occupancy of site (i,j). The first term on the right of Eq. (4) represents the change in occupancy of site (i,j) caused by a motility event where an agent moves in the positive x direction, and the right-most end of this agent moves into site (i,j). All other terms in Eq. (4) can be interpreted in a similar way.

The discrete conservation statement is related to a PDE model in the appropriate limit as $\Delta \to 0$ and $\tau \to 0$ simultaneously, and discrete values of $\langle C_{i,j}\rangle$ are written in terms of a continuous variable $C(x,y,t)$. To see this relationship, all terms in Eq. (4) are expanded in a Taylor series about (i,j). These Taylor series are truncated so that we neglect terms of $\mathcal{O}(\Delta)^3$ and higher. Dividing the resulting expression by τ, we then take limits as $\Delta \to 0$ and $\tau \to 0$ jointly, with the ratio (Δ^2/τ) held constant [32]. In the continuum limit we obtain a PDE that can be written as

$$\frac{\partial C}{\partial t} = D_0\frac{\partial}{\partial x}\left[D_x(C)\frac{\partial C}{\partial x}\right] + D_0\frac{\partial}{\partial y}\left[D_y(C)\frac{\partial C}{\partial y}\right], \quad D_x(C) = L^2C^{L-1}, \quad D_y(C) = L^2[C(1-C)]^{L-1}, \quad (5)$$
$$D_0 = \frac{P_m}{4}\lim_{\Delta,\tau\to 0}\left(\frac{\Delta^2}{\tau}\right).$$

This is a key result as the limiting PDE model is a nonlinear diffusion equation that is degenerate in the sense that $D_x(0) = D_y(0) = 0$ for $L \geqslant 2$. This is similar to the PME except that here we have anisotropic nonlinear diffusivity functions with $D_x(C) \neq D_y(C)$ for $L \geqslant 2$, whereas for the PME we have isotropic nonlinear diffusivity functions with $D_x(C) = D_y(C)$ [8,9]. The anisotropic nonlinear diffusivity functions in Eq. (5) reflect the fact that crowding effects in a population of horizontally aligned agents with $L \geqslant 2$ mean that the ability of an agent to move horizontally is not the same as the ability of an agent to move in the vertical direction. We also see that Eq. (5) relaxes to a linear diffusion model when $L = 1$ [22,29] since $D_x(C) = D_y(C) = 1$ in this case.

The PDE model given by Eq. (5) is relevant in the limit as $\Delta \to 0$ and $\tau \to 0$ simultaneously while holding the ratio (Δ^2/τ) constant [32,33]. To apply this model to a particular biological system we set the lattice spacing equal to the cell diameter [26–28,34]. In dimensional variables, using * to represent dimensional quantities, Δ^* is approximately 10–20 μm [28,34]. To select the dimensional time step τ^*, we interpret τ^* as an inspection time after which the location of an isolated agent is recorded. By making a large number of repeated inspections, separated by the time interval τ^*, we can infer the probability that an isolated agent undergoes a motility event during the interval τ^* as $P_m \in [0,1]$. Rather than specifying the dimensional inspection time τ^* and the probability of motility P_m separately, it is more relevant to specify their ratio P_m/τ^*, which is a measure of the probability that an isolated agent undergoes a motility event during any particular inspection period regardless of the length of that period. This means that the individual values of P_m and τ^* do not uniquely specify the motility rate; rather, it is the ratio P_m/τ^* that uniquely determines the agent motility. Without loss of generality, we always work with dimensionless simulations by setting $\Delta = \tau = 1$. In this way, the nondimensional time step can be rescaled to any particular dimensional time step τ^* without difficulty. Similarly, the nondimensional lattice spacing can be rescaled to the appropriate dimensional lattice spacing Δ^*. Given that the continuum-discrete comparisons we present in Secs. II D and II F all show a good correspondence between the discrete data and the solution of the corresponding continuum models, we conclude that nondimensional simulations with $\Delta = \tau = 1$ are appropriate for studying the continuum limit of these discrete mechanisms. These nondimensional simulations can then be simply rescaled to represent any particular application of the model.

D. Continuum-discrete comparison: One-dimensional spreading

To test how the PDE model predicts the movement of a population of horizontally aligned agents, we consider the simulation data in Figs. 3(d)–3(g). The configuration of these simulations reduces the system to a one-dimensional problem as previously described in Sec. II A [22]. Accordingly, we compare the column density of agents, averaged over many simulations, with the numerical solution of a one-dimensional form of Eq. (5):

$$\frac{\partial C}{\partial t} = D_0\frac{\partial}{\partial x}\left[D_x(C)\frac{\partial C}{\partial x}\right]. \quad (6)$$

The numerical solution of Eq. (6) is obtained using a finite difference approximation with constant grid spacing δx and implicit Euler stepping with constant time steps δt. Picard linearization, with absolute error tolerance ϵ, is used to solve the resulting nonlinear algebraic systems [35]. We solve Eq. (6) on $1 \leqslant x \leqslant 400$ with reflecting boundary conditions at $x = 1$ and $x = 400$ and an initial condition given by

$$C(x,0) = H(x_L) - H(x_R), \quad (7)$$

where H is the Heaviside function and x_L and x_R are chosen so that the initial condition for the continuum model matches the initial condition for the discrete simulations. For $L = 1,2,3,4$, we choose $(x_L,x_R) = (181,220),(181,220),(181,219),(181,220)$, respectively. Numerical solutions of Eqs. (6)–(7) are superimposed on the discrete profiles in Figs. 3(d)–3(g). The solution profiles of Eqs. (6)–(7) are symmetric about $x = x_0 = (x_L + x_R)/2$. For $L \geqslant 2$ these solutions have compact support on $-s(t) < x - x_0 < s(t)$, where $x = x_0 \pm s(t)$ describes the location of the interface where $C(x,t) = 0$ [8,9]. In Sec. II E we will derive an analytical expression for the interface location $x = x_0 \pm s(t)$.

Comparing the solution of Eqs. (6)–(7) with the simulation data shows that we have an excellent match when $L = 1$. This is a known result that has been demonstrated previously [22]. More interestingly, we see that for $L \geqslant 2$, the solution of Eqs. (6)–(7) also matches the simulation data reasonably well. In particular, for $L \geqslant 2$ the solution of Eqs. (6)–(7) accurately predicts the evolution of the density profiles in regions of the lattice where $C(x,t) \not\approx 0$. On the other hand, the continuum-discrete comparison is not as good near the interface $x = x_0 \pm s(t)$ where the solution of the PDE is sharp fronted [8,9]. The discrepancy between the simulation data and the solution of Eq. (6) in this neighborhood increases as L increases.

There are at least two possible reasons why we observe the discrepancy between the continuum and discrete profiles as L increases. First, when we derived the continuum model we made the initial assumption that the occupancy of lattice sites could be related using a truncated Taylor series expansion. The Taylor series relating the occupancy of sites $(i + a, j + b)$ and (i, j) is given by

$$C_{i+a,j+b} = C_{i,j} + \frac{(a\Delta)^1}{1!}\frac{\partial C_{i,j}}{\partial x} + \frac{(b\Delta)^1}{1!}\frac{\partial C_{i,j}}{\partial y} + \frac{(a\Delta)^2}{2!}\frac{\partial^2 C_{i,j}}{\partial x^2} + \frac{2ab\Delta^2}{2!}\frac{\partial^2 C_{i,j}}{\partial x \partial y} + \frac{(b\Delta)^2}{2!}\frac{\partial^2 C_{i,j}}{\partial y^2} + \mathcal{O}(\Delta^3), \tag{8}$$

where $a, b \in \mathbb{Z}$. By using Eq. (8), we implicitly assumed that the corresponding solution of the governing PDE, $C(x,y,t)$, was sufficiently differentiable so that the density profile could be expanded in a Taylor series. It is only in retrospect, after forming the PDE model, that we know the solution of the PDE will be smooth for $L = 1$ since this case gives rise to the linear diffusion equation. However, when $L \geqslant 2$, the governing PDE model turns out to be a degenerate nonlinear diffusion equation that can support sharp-fronted solutions [8,9]. These sharp-fronted solutions are not differentiable at the interface $x = x_0 \pm s(t)$ but are but are differentiable elsewhere. Given that our discrete-continuum comparison shows that the PDE matches the simulation in all locations except near the interface $x = x_0 \pm s(t)$, this appears to be a plausible explanation for the discrepancy between the continuum and discrete models.

Second, the discrepancy between the continuum and discrete models could also be due to the failure of the independence assumption underlying the discrete conservation statement (Eq. (4)). To form the conservation statement, we assume that the occupancy status of lattice sites are independent. This is a standard assumption made by us [22–24] and others [25,36] and it allows us to interpret products of various occupancy (or vacancy) probabilities as a net transition probability. Intuitively, the independence assumption becomes less appropriate as L increases. For example, consider a single agent with $L = 1$ located at (i, j). If this agent attempts to move in the positive x direction, the discrete conservation statement requires that we treat the occupancy of sites (i, j) and $(i + 1, j)$, averaged over many identically prepared realizations, as independent. In comparison, if we consider an agent with $L = 4$ occupying sites $(i - 3, j)$, $(i - 2, j)$, $(i - 1, j)$, and (i, j), and that agent moves in the positive x direction, the conservation statement requires us to treat the occupancy of sites $(i - 3, j)$, $(i - 2, j)$, $(i - 1, j)$, (i, j), and $(i + 1, j)$, averaged over many identically prepared realizations, as independent. This independence assumption is less satisfactory for $L = 4$ than for $L = 1$, and, in general, the independence assumption becomes less appealing as L increases. Therefore, this assumption could also contribute to the decrease in the quality of the continuum-discrete comparison as L increases (Fig. 3). Although we are making progress toward understanding how to relax the independence assumption for spatially uniform problems [37], considerable work remains to understand how to relax the independence assumption for spatially variable problems.

E. Analytical approximations

Although we observe a slight discrepancy between the discrete and continuum models near the interface $x = x_0 \pm s(t)$, and note that this discrepancy increases with L, the overall comparison between the continuum and discrete data is good; even with $L = 4$, the continuum PME model accurately predicts the averaged agent distribution near $x = x_0$. Given this demonstrated relationship, we now make use of certain analytical results to gain further insight into the discrete model. In addition to the numerical solutions of Eqs. (6)–(7), which we denote $C(x,t)$, Eq. (6) has an exact similarity solution [8,9], which we denote $C_s(x,t)$. The similarity solution is relevant for $-\infty < x < \infty$ with a source-type initial condition $C_s(x,0) = m\delta(x - x_0)$, where $m = \int_{-\infty}^{\infty} C_s(x,t)\,dx$. The source solution can be written as

$$C_s(x,t) = \frac{1}{(t - t_0)^{1/(L+1)}}\left\{\frac{2(L-1)}{P_m L^2 (L+1)} \times \left[a^2 - \frac{(x - x_0)^2}{(t - t_0)^{2/(L+1)}}\right]\right\}^{1/(L-1)}, \quad L \geqslant 2, \tag{9}$$

where the constant a is given by

$$a = \left[\frac{P_m L^2 (L+1)}{2(L-1)}\right]^{1/(L+1)} \left\{\frac{m\,\Gamma\left[\frac{3L-1}{2(L-1)}\right]}{\sqrt{\pi}\,\Gamma\left(\frac{L}{L-1}\right)}\right\}^{(L-1)/(L+1)}, \tag{10}$$

with $\Gamma(z)$ indicating the Gamma function. Here x_0 and t_0 are shifts in space and time, reflecting the invariance of Eq. (6) under translation in both space and time. This source solution represents spreading mound-shaped profiles centered at $x = x_0$, with compact support over a finite domain. For large L these profiles are mesa-shaped with steep sides and flat tops. For the same source-type problem with linear diffusion, the analogous solution is [31]

$$C_s(x,t) = \frac{m e^{-(x-x_0)^2/P_m(t-t_0)}}{\sqrt{\pi P_m (t - t_0)}}, \quad L = 1, \tag{11}$$

which is a Gaussian curve that does not have compact support.

The source-type solutions, $C_s(x,t)$, are an excellent approximation to the solution of Eqs. (6)–(7) despite

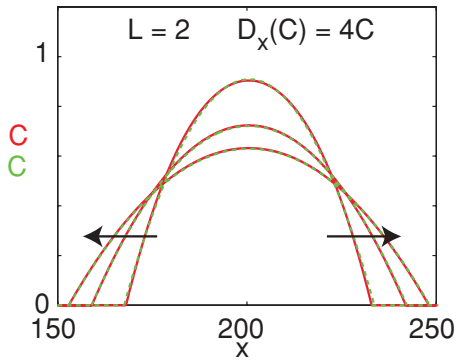

FIG. 5. (Color online) Comparison of the numerical solution of Eqs. (6)–(7), shown in red (solid), and the source solution Eq. (10), shown in green (dotted), for $L = 2$ and $P_m = 1$. Numerical solutions of Eq. (6) are shown at $t = 100,300,500$ for an initial condition with $C(x,0) = 1$ for $180 \leqslant x \leqslant 219$ and $C(x,0) = 0$ elsewhere on $0 \leqslant x \leqslant 400$. The source solution is superimposed using appropriate time and space shifts, $x_0 = 200.5$ and $t_0 = 100$. The arrows show the direction of increasing t.

differences in the initial distributions, $C(x,0)$ and $C_s(x,0)$. Formally, we have [8,9,38]

$$C(x,t) \sim C_s(x,t) \quad \text{as} \quad t \to \infty. \tag{12}$$

For intermediate times a good approximation is found with appropriate values x_0 and t_0. For example, in Fig. 5 we compare numerical solutions of Eqs. (6)–(7) for $L = 2$ [the problem previously described in Fig. 3(f)] with the source solution, Eqs. (9)–(10), for three representative times, with the choice $x_0 = (x_L + x_R)/2$ and $t_0 = 100$. This choice for x_0 is simply the center of the initial distribution. The shift in time t_0 was chosen using a trial-and-error approach where we visually matched the analytical and numerical results. The numerical-analytical comparison, given in Fig. 5, is extremely good and improves as t increases. The high quality of the numerical-analytical comparison negates any need for sophisticated methods to determine t_0, especially given that Eq. (12) holds regardless of the value of t_0 [8,9,38].

A further use of the source solution is that it provides analytical insight into the time dependence of the profiles in Fig. 3. For example, the location of the moving front $x = x_0 \pm s(t)$ is formally connected to the source solution via [8,9]

$$s(t) - x_0 \sim a(t - t_0)^{1/(L+1)} \quad \text{as} \quad t \to \infty, \quad L \geqslant 2; \tag{13}$$

again, for intermediate times the approximation (13) is extremely good, especially after careful choice of t_0. In the linear diffusion case, $L = 1$, there are no moving fronts, and information is effectively propagating with infinite speed; on the other hand, the power-law relationship (Eq. (13)) shows explicitly that the front speed is finite for $L \geqslant 2$ and that this speed decreases as L increases. Further, the source solution shows that the peaks of the spreading profiles at $x = x_0$ in Figs. 3 and 5 decrease in height according to

$$C(x_0,t) \sim \left[\frac{2(L-1)a^2}{P_m L^2(L+1)}\right]^{1/(L-1)} (t - t_0)^{-1/(L+1)} \quad \text{as} \quad t \to \infty, \quad L \geqslant 2;$$

that is, the height, $C(x_0,t)$, decreases more quickly as L increases. This is consistent with our previous observations of the density profiles extracted from the simulations (Fig. 3).

Finally, we make the point that the source-type solutions to Eq. (6) are valid on $-\infty < x < \infty$. In order to facilitate the numerical-analytical comparison we had to generate numerical solutions on a truncated finite domain with $1 \leqslant x \leqslant 400$. Comparing analytical solutions that are valid on an infinite domain with numerical solutions on a truncated domain is a standard approach used when testing and validating the performance of a numerical code. This approach has been used by us [39] and others [40] and is valid for sufficiently small times where the numerical solution on the truncated finite domain does not interact with the boundary conditions applied at the ends of the domain.

F. Continuum-discrete comparison: Two-dimensional spreading

To complement the one-dimensional simulation data in Fig. 3, we also present two-dimensional data in Fig. 6 on a lattice with $1 \leqslant x \leqslant 200$ and $1 \leqslant y \leqslant 200$. We consider two initially close-packed horizontally aligned populations. In the first case we consider a population with $L = 2$, and agents are initially placed so that all sites with $75 \leqslant x \leqslant 124$ and $75 \leqslant y \leqslant 124$ are occupied by $N = 1250$ agents, as shown in Fig. 6(a). Reflecting boundary conditions are imposed along all boundaries. Simulation data in Figs. 6(a)–6(b), show how the population of agents spreads over time. For this particular geometry, the double average used to collapse the two-dimensional data into one-dimensional density profiles in Sec. II A is inappropriate, and we must consider a more general average [22]. If $C^m(i,j)$ is the occupancy of site (i,j) during the mth realization, then the average occupancy of site (i,j) is given by

$$\langle C(x,y,t)\rangle = \frac{1}{M}\sum_{m=1}^{M} C^m(i,j). \tag{14}$$

To generate two-dimensional density data from these simulations we considered $M = 100$ identically prepared realizations to approximate $\langle C(x,y,t)\rangle$, using Eq. (14). This averaged data were contoured using standard MATLAB routines. Numerical solutions of Eq. (5), with initial and boundary conditions to match the discrete simulations, were also generated and contoured. The continuum and discrete contours are superimposed in Fig. 6(c), showing an excellent match.

In the second case we consider a population with $L = 4$, and agents are initially placed so that all sites with $75 \leqslant x \leqslant 122$ and $75 \leqslant y \leqslant 122$ are occupied by $N = 576$ agents, as shown in Fig. 6(d). Reflecting boundary conditions are imposed along all boundaries. Simulation data in Figs. 6(d)–6(e), show how the population of agents spreads over time. To generate two-dimensional contour data, we considered $M = 100$ identically prepared realizations to approximate $\langle C(x,y,t)\rangle$ at $t = 300$ using Eq. (14). Corresponding numerical solutions of Eq. (5) are superimposed in Fig. 6(f), showing a good match. By comparing the continuum-discrete match in Figs. 6(c) and 6(f), we see that the $\langle C(x,y,t)\rangle = 0.75$ contours match very well for both the $L = 2$ and $L = 4$ populations. In comparison, if we compare the $\langle C(x,y,t)\rangle = 0.50$ contour,

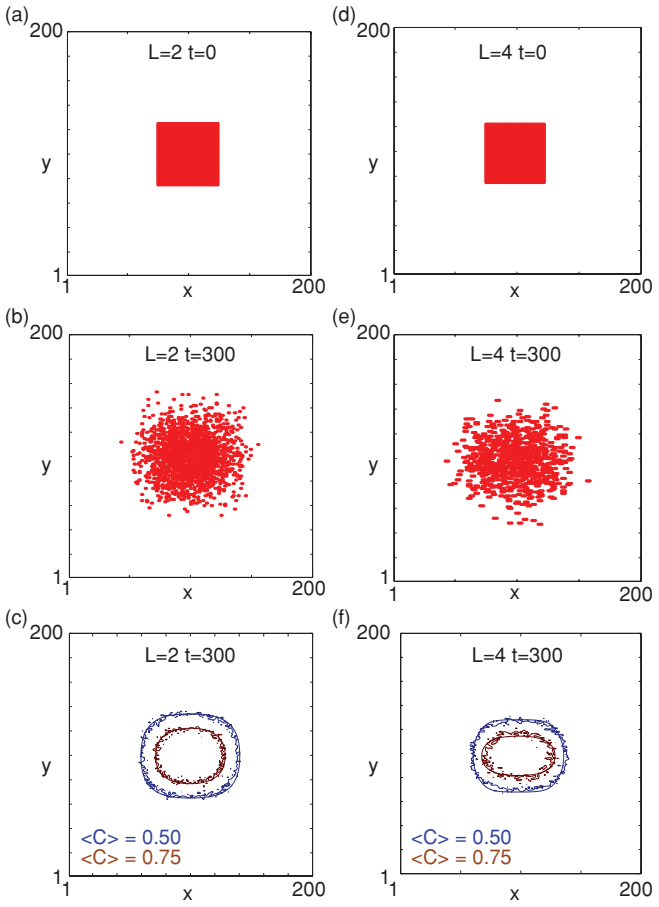

FIG. 6. (Color online) (a) Two-dimensional simulations start with all sites occupied where $75 \leqslant x,y \leqslant 124$ so that this region is completely occupied by $N = 1250$ horizontally aligned agents with $L = 2$. (b) A snapshot of a single realization at $t = 300$ for $P_m = \Delta = \tau = 1$. (c) The $\langle C(x,y,t)\rangle = 0.50$ contour is shown in blue (light gray), and the $\langle C(x,y,t)\rangle = 0.75$ contour is shown in brown (dark gray). These contours are obtained from the discrete model, averaged over $M = 100$ identically prepared realizations. The discrete contours are superimposed on the equivalent contour data taken from a numerical solution of Eq. (5). (d) Two-dimensional simulations start with all sites occupied where $75 \leqslant x,y \leqslant 122$ so that this region is completely occupied by $N = 576$ horizontally aligned agents with $L = 4$. (e) A snapshot of a single realization at $t = 300$ for $P_m = \Delta = \tau = 1$. (f) The $\langle C(x,y,t)\rangle = 0.50$ contour is shown in blue (light gray), and the $\langle C(x,y,t)\rangle = 0.75$ contour is shown in brown (dark gray). These contours are obtained from the discrete model, averaged over $M = 100$ identically prepared realizations. The discrete contours are superimposed on the equivalent contour data taken from a numerical solution of Eq. (5). In all cases the solution of Eq. (5) is obtained numerically using the method described in the text with an initial condition and boundary conditions that matches the discrete simulations. Numerical solutions of Eq. (5) are obtained with $\delta x = \delta y = 0.5$, $\delta t = 0.25$, and $\epsilon = 1 \times 10^{-6}$.

we see an excellent match for the $L = 2$ population, whereas the match for the $L = 4$ population is not as good. This observation is consistent with the results in Fig. 3 where we saw that the continuum-discrete match became less satisfactory as L increased and the continuum-discrete match was less satisfactory in the low-density region of the lattice near the leading edge of the population. Despite this observation, we conclude that comparing the discrete-continuum contours in Fig. 6 shows that the two-dimensional discrete contours match the solution of Eq. (5).

Both the simulation data and the solution of Eq. (5) (Fig. 6) show an anisotropic distribution of agents: The contours are elongated in the x direction relative to the y direction. This anisotropy is a consequence of the anisotropic crowding effects. For example, an agent in Fig. 6(a) attempting to move in the x direction requires one adjacent site to be vacant for that motility event to be successful. In comparison, an agent in Fig. 6(a) attempting to move in the y direction requires two adjacent sites to be vacant for that motility event to be successful. Therefore, it is not surprising that we see the contours in Fig. 6(c) elongated in the x direction. We see more pronounced anisotropic spreading in Fig. 6(f) for the $L = 4$ population because the anisotropic crowding effects are more pronounced as L increases. Unfortunately, this anisotropic spreading cannot be analyzed analytically with a similarity solution since Eq. (5) does not admit any useful similarity reduction. Now that we have demonstrated that it is possible to compare discrete and continuum models using either one- or two-dimensional data, for simplicity we will present only one-dimensional data from this point forward.

III. A POPULATION COMPOSED OF DIFFERENTLY ALIGNED AGENTS

A. Discrete simulations

We have presented a biologically motivated argument suggesting that the PME plays a role in describing the collective movement of rod-shaped agents. However, in the previous section we assumed that the entire population was uniformly aligned. To relax this assumption, we now present simulation results and corresponding continuum models that describe a population of agents composed of a horizontally aligned subpopulation that interacts with a vertically aligned subpopulation. Both subpopulations have $L \geqslant 2$ and undergo motility events and rotation events that maintain volume exclusion. Column-averaged density profiles, which are further averaged over many identically prepared realizations, are denoted $\langle C_h(x,t)\rangle$ and $\langle C_v(x,t)\rangle$ for the horizontal and vertical subpopulations, respectively. Similarly, the continuum density profiles for the horizontally aligned subpopulation and the vertically aligned subpopulation are denoted $C_h(x,t)$ and $C_v(x,t)$, respectively. Figure 7(a) shows a lattice fragment where sites $(i, j-1)$ and $(i+1, j-1)$ are occupied by a horizontal agent, while sites $(i+1, j)$ and $(i+1, j+1)$ are occupied by a vertical agent.

Each subpopulation undergoes motility events with probability $P_m \in [0,1]$ in the same way as described previously for the single population case. In addition to motility events, we now allow each subpopulation to rotate around an angle of $\pm\pi/2$. These rotation events convert members of one subpopulation into members of the other subpopulation during the simulation. Rotations occur with probability $P_r \in [0,1]$. The discrete algorithm for marching the system forward a single time step of length τ consists of four steps that can be

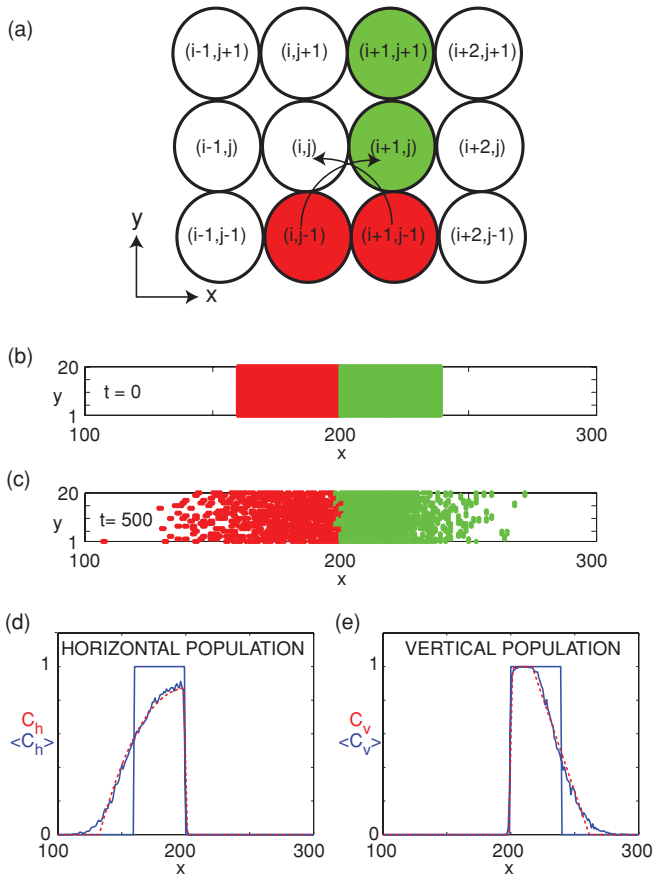

FIG. 7. (Color online) (a) A portion of lattice that is partly occupied by a two agents, each with $L = 2$. The agent parallel with the x axis is shown in red (dark gray) and occupies sites $(i, j-1)$ and $(i+1, j=1)$, while the agent parallel to the y axis is shown in green (light gray) and occupies sites $(i+1, j)$ and $(i+1, j+1)$. (b)–(c) Simulation data for a system without rotation for $P_m = \Delta = \tau = 1$ and $P_r = 0$. The horizontal subpopulation is originally distributed so that each column between $160 \leqslant x \leqslant 199$ is completely occupied giving 20 adjacent columns of nonoverlapping agents that are parallel to the x axis, each with $L = 2$. The vertical subpopulation is originally distributed so that each column $200 \leqslant x \leqslant 239$ is completely occupied, giving 40 adjacent columns of nonoverlapping agents that are parallel to the y axis, each with $L = 2$. Snapshots of a single realization at $t = 0$ and $t = 500$ are shown in (b)–(c), respectively. (d)–(e) Column-averaged occupancy data averaged over $M = 100$ identically prepared realizations for the horizontal subpopulation $\langle C_h(x,t)\rangle$ and the vertical subpopulation $\langle C_v(x,t)\rangle$, respectively, at $t = 0$ and $t = 500$ are shown in blue (solid). Numerical solutions of a one-dimensional form of Eq. (15)–(16), $C_h(x,t)$ and $C_v(x,t)$, are shown in red (dotted) at the same time points using initial and boundary conditions that match the discrete simulations. Numerical solutions are obtained using $\delta x = 0.1$, $\delta t = 0.01$, and $\epsilon = 1 \times 10^{-6}$.

described as follows: (i) If there are N_h horizontal agents on the lattice, then N_h horizontal agents are selected independently at random, one at a time. When chosen, a horizontal agent attempts to move with probability $P_m \in [0,1]$. (ii) If there are N_v vertical agents on the lattice, then N_v vertical agents are selected independently at random, one at a time. When chosen, a vertical agent attempts to move with probability $P_m \in [0,1]$. (iii) If there are N_h horizontal agents on the lattice, then N_h horizontal agents are selected independently at random, one at a time. When chosen, a horizontal agent attempts to rotate with probability $P_r \in [0,1]$. (iv) If there are N_v vertical agents on the lattice, then N_v vertical agents are selected independently at random, one at a time. When chosen, a vertical agent attempts to rotate with probability $P_r \in [0,1]$. Once these four steps have been completed, we increment time from t to $t + \tau$. We note that in general, the values of N_h and N_v can change during each time step for $P_r > 0$. Our approach is appropriate for small values of P_r where the change in the values of N_h and N_v are small per time step [24]. Separating the motility and rotation events like this is similar to an operator splitting method for solving continuum reaction diffusion equations [39]. In addition to this simple time marching algorithm, we also simulated all discrete results presented in this paper using a more sophisticated Gillespie algorithm [41] and found that the simple time marching algorithm and the Gillespie algorithm gave indistinguishable results for the parameter values presented here.

For any rotation event, the agent attempts to pivot about one of the lattice sites occupied by that particular agent. For simplicity we choose the pivot site randomly so that each site occupied by the agent has an equal probability of acting as the pivot site. Once the pivot site is chosen, the agent must then choose a rotation direction, and for simplicity we will choose the rotation direction so that either clockwise or anticlockwise rotations are equally likely. This means that each agent of length L can potentially undergo $2L$ different rotation events. These potential rotation events are only permitted provided that volume exclusion is maintained. In particular, we only allow rotation events when the final state as well as the intermediate state(s) of the rotation event ensure that volume exclusion is maintained. For example, the green agent in Fig. 7(a) could undergo one of four different types of rotations: (i) pivot clockwise about $(i+1, j)$ to become a horizontal agent occupying sites $(i+1, j)$ and $(i+2, j)$, (ii) pivot anticlockwise about $(i+1, j)$ to become a horizontal agent occupying sites (i, j) and $(i+1, j)$, (iii) pivot clockwise about $(i+1, j+1)$ to become a horizontal agent that occupies sites $(i, j+1)$ and $(i+1, j+1)$, or (iv) pivot anticlockwise about $(i+1, j+1)$ to become a horizontal agent that occupies sites $(i+1, j+1)$ and $(i+2, j+1)$. For the configuration shown in Fig. 7(a), any of these four rotation events would be permitted because the target site and all other intermediate sites encountered by that green agent during the potential rotation event are vacant. In comparison, if we consider the potential rotation events for the red agent in Fig. 7(a) we see that a clockwise rotation about site $(i+1, j-1)$ (illustrated with a clockwise arrow) would be aborted because the target site $(i+1, j)$ is occupied. Similarly, an anticlockwise rotation about site $(i, j-1)$ (illustrated with an anticlockwise arrow) would not be permitted. This is because, as the red agent pivots anticlockwise about site $(i, j-1)$, part of the red agent that initially occupies site $(i+1, j-1)$ would rotate across site $(i+1, j)$. For the configuration shown in Fig. 7(a), site $(i+1, j)$ is occupied, and hence this rotation event would not maintain volume exclusion.

To implement these rotation events in the discrete algorithm we assessed each rotation event separately by ensuring that two

conditions were satisfied. First, the algorithm checked that the final target site(s) associated with each particular rotation event of interest were vacant. Second, the algorithm checked that all intermediate sites that the agent would rotate across during the rotation event were vacant. Only if all the target sites and all intermediate sites are vacant is the particular rotation event permitted.

B. A continuum model

Using this rotation mechanism, together with the motility mechanism described previously for the single population model, we can now write down conservation of occupancy statements for both the horizontal, $\langle C_h(x,y,t)\rangle$, and the vertical, $\langle C_v(x,y,t)\rangle$, subpopulations that are analogous to Eq. (4). Accounting for all possible interactions, expanding all terms using truncated Taylor series about site (i,j) and considering the limits as $\Delta \to 0$ and $\tau \to 0$, again keeping (Δ^2/τ) constant, we obtain the following system of coupled PDEs:

$$\begin{aligned}\frac{\partial C_h}{\partial t} &= D_0 L^2 \frac{\partial}{\partial x}\left[C_h^{(L-1)}(1-C_v)\frac{\partial C_h}{\partial x}\right] \\ &+ D_0 L^2 \frac{\partial}{\partial x}\left(C_h^L \frac{\partial C_v}{\partial x}\right) \\ &+ D_0 L^2 \frac{\partial}{\partial y}\left[C_h^{(L-1)}(1-C_v)(1-C_v-C_h)^{(L-1)}\frac{\partial C_h}{\partial y}\right] \\ &+ D_0 L^2 \frac{\partial}{\partial y}\left[C_h^L(1-C_h-C_v)^{(L-1)}\frac{\partial C_v}{\partial y}\right] \\ &+ \rho(L-1)(1-C_h-C_v)^{L(L-1)}\left(C_v^L - C_h^L\right), \qquad (15)\end{aligned}$$

$$\begin{aligned}\frac{\partial C_v}{\partial t} &= D_0 L^2 \frac{\partial}{\partial x}\left[C_v^L(1-C_h-C_v)^{(L-1)}\frac{\partial C_h}{\partial x}\right] \\ &+ D_0 L^2 \frac{\partial}{\partial x}\left[C_v^{(L-1)}(1-C_h)(1-C_v-C_h)^{(L-1)}\frac{\partial C_v}{\partial x}\right] \\ &+ D_0 L^2 \frac{\partial}{\partial y}\left(C_v^L \frac{\partial C_h}{\partial y}\right) \\ &+ D_0 L^2 \frac{\partial}{\partial y}\left[C_v^{(L-1)}(1-C_h)\frac{\partial C_v}{\partial y}\right] \\ &- \rho(L-1)(1-C_h-C_v)^{L(L-1)}\left(C_v^L - C_h^L\right), \qquad (16)\end{aligned}$$

where

$$D_0 = \frac{P_m}{4}\lim_{\Delta,\tau\to 0}\left(\frac{\Delta^2}{\tau}\right), \quad \rho = \lim_{\tau\to 0}\left(\frac{P_r}{\tau}\right). \qquad (17)$$

These equations are complicated nonlinear advection-diffusion-reaction equations describing the evolution of the two subpopulation densities. We see that the source terms in Eqs. (15)–(16) are equal in magnitude and opposite in sign, ensuring that the total agent density, $C(x,y,t) = C_h(x,y,t) + C_v(x,y,t)$, is conserved. This is expected: although we allow both subpopulations to rotate and transform from horizontal to vertical agents, or alternatively from vertical to horizontal agents, the total number of agents present on the lattice remains fixed with time so the total agent density is conserved.

The condition that $\rho = \lim_{\tau\to 0}(\frac{P_r}{\tau})$ implies that for our simulation data to match the PDE models we require $P_r = \mathcal{O}(\tau)$ so that ρ is finite [24,32,33]. Accordingly, we expect that the continuum PDE model will be valid for small values of P_r only. We have previously found that a similar condition applies to models of agent proliferation where we require that the proliferation rate be sufficiently small for the continuum model to be valid [24]. Therefore we will only attempt to match simulation data and solutions of the continuum model for small values of P_r.

C. Continuum-discrete comparison: One-dimensional spreading

To demonstrate the performance of Eqs. (15)–(16) we first generated discrete results shown in Figs. 7(b)–7(c) for no rotation ($P_m = 1, P_r = 0$). The horizontal subpopulation is originally distributed so that each column between $160 \leqslant x \leqslant 199$ is completely occupied giving 20 columns of adjacent nonoverlapping horizontal agents, each with $L = 2$. This means that initially we have $N_h = 400$ horizontal agents. The vertical subpopulation is originally distributed so that each column $200 \leqslant x \leqslant 239$ is completely occupied giving 40 columns of adjacent nonoverlapping vertical agents, each with $L = 2$. This means that initially we have $N_v = 400$ vertical agents. Snapshots of a single realization at $t = 0$ and $t = 500$ are shown in Figs. 7(b)–7(c), respectively. We see that both subpopulations are able to move away from the initially close-packed distribution. Comparing the column-averaged density profiles extracted from $M = 100$ identically prepared realizations ($\langle C_h(x,t)\rangle$, $\langle C_v(x,t)\rangle$) with the solution of Eqs. (15)–(16) ($C_h(x,t)$, $C_v(x,t)$) for initial and boundary conditions that match the discrete simulations, we see that the continuum model does an excellent job of predicting the averaged behavior of the discrete simulations. In general we observe that the interface between the two subpopulations at $x = 200$ remains sharp while the horizontal subpopulation moves in the direction of decreasing x and the vertical subpopulation moves in the direction of increasing x. Similar to the results for the single population of horizontally aligned agents (Fig. 3), we see that the match between the PDE model and the discrete data is very good except near the leading edges of the profile where both the continuum solutions for $C_h(x,t)$ and $C_v(x,t)$ are sharp fronted. We also observe that the horizontal subpopulation is more mobile than the vertical subpopulation. For example, by $t = 500$, the horizontal agents have been able to move so that $\langle C_h(x,t)\rangle < 1$ everywhere across the lattice. In comparison, by $t = 500$ the vertical agents have been less successful at moving, and we still observe $\langle C_v(x,t)\rangle = 1$ in the region $200 \leqslant x \leqslant 225$. This unequal spreading is caused by the anisotropic nature of the crowding effects that previously gave rise to the anisotropic density contours in Fig. 6.

In Figs. 8(a)– 8(d) we present similar results for the same problem described in Fig. 7 but now with a small rotation rate ($P_m = 1, P_r = 0.01$). In this case we observe the distribution of agents in a single realization in Figs. 8(a)– 8(b) at $t = 0$ and $t = 500$, respectively. These snapshots clearly show the influence of the rotation events. At the leading edge of the horizontal subpopulation, which is attempting to move in the negative x direction, there is sufficient space available to allow certain rotation events that gives rise to a number of

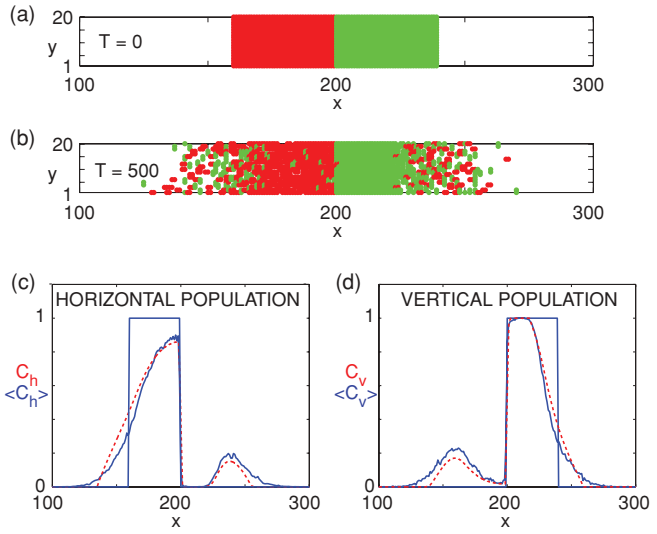

FIG. 8. (Color online) (a)–(b) Simulation data for a system with rotation for $P_m = \Delta = \tau = 1$ and $P_r = 0.01$. The initial condition is the same as in Fig. 7. Snapshots of a single realization at $t = 0$ and $t = 500$ are shown in (a)–(b), respectively. (c)–(d) Column-averaged occupancy data averaged over $M = 100$ identically prepared realizations for the horizontal subpopulation, $\langle C_h(x,t)\rangle$, and the vertical subpopulation, $\langle C_v(x,t)\rangle$, respectively, at $t = 0$ and $t = 500$ are shown in blue (solid). Numerical solutions of a one-dimensional form of Eq. (15)–(16) are shown in red (dotted) at the same time points using initial and boundary conditions that match the discrete simulations. Numerical solutions are obtained using $\delta x = 0.1$, $\delta t = 0.01$, and $\epsilon = 1 \times 10^{-6}$.

vertical agents. Similarly, at the leading edge of the vertically aligned subpopulation, which is attempting to move in the positive x direction, there is sufficient space available to allow certain rotation events that gives rise to a number of horizontal agents. Comparing the column averaged density profiles extracted from $M = 100$ identically prepared realizations ($\langle C_h(x,t)\rangle$, $\langle C_v(x,t)\rangle$) with the solution of the corresponding continuum model ($C_h(x,t)$, $C_v(x,t)$) shows that the continuum model captures the essential features of the discrete simulations. In general, however, the continuum-discrete comparison in Fig. 8 is not as good as in Fig. 7. There are two possible reasons for this. First, the continuum models are strictly valid in the limit $\tau \to 0$ with $P_r = \mathcal{O}(\tau)$, meaning that the rotation rate must be sufficiently small. Although we present results for $P_r = 0.01$, we also generated results for $P_r = 0.001$ and observed an improved continuum-discrete match. Of course, setting $P_r = 0.001$ means that there are far less rotation events, and these results did not demonstrate the effects of rotations as much as the simulations in Fig. 8 with $P_r = 0.01$. Second, even with $P_r = 0$ (Fig. 7) we see that there is a small discrepancy between the continuum and discrete profiles at the leading edge where the continuum profiles are sharp fronted. All of our results show a small discrepancy in this region which is the same region where rotations are likely to occur because there is sufficient space. In general, the discrepancy between the continuum and discrete profiles could arise due to a combination of these two effects. Nevertheless, the continuum models successfully predict the main features of the discrete simulations.

IV. DISCUSSION AND CONCLUSIONS

Multiscale modeling of cell biology processes is critical because experimental data often comprise both population-level (macroscopic) and individual-level (microscopic) measurements [21]. These complicated observations are difficult to integrate into a modeling study that uses a single-scale model in isolation. As a result, there is great interest in being able to describe a model of cellular processes both from the viewpoint of a single cell and a population of cells [6,25,42,43]. Our work is primarily focused on investigating cell motility mechanisms that appear relevant at the level of an individual cell and then analyzing the discrete motility mechanism to understand the resulting population-level response in terms of the corresponding continuum model.

Previous applications of exclusion process models to collective cell spreading problems have all made the assumption that cells can be represented as round agents that move on a lattice so that each agent occupies a single lattice site [22,26–28,34]. Our current work is motivated by the observation that cells are often rod shaped and elongated (Fig. 2(a)). To model the collective motion of a population of interacting cells, we consider a generalized exclusion process model where each cell is represented by an agent. Agents reside on a lattice, and each agent can occupy $L \geqslant 1$ adjacent lattice sites. By making standard assumptions, we use conservation principles to arrive at a continuum description of the collective motion of a population of rod-shaped agents. We confirm the well-known result that "round" agents ($L = 1$) correspond to a linear diffusion mechanism whereas elongated rod-shaped agents $L \geqslant 2$ obey a degenerate nonlinear diffusion equation that is related to the PME. Comparing average density data from the simulations with numerical solutions of the corresponding continuum PDE models shows that the continuum models derived here can accurately describe the mean behavior of the discrete models.

Certain previous modeling approaches have considered different ways to represent the influence of varying cell shape and cell size. For example, the work of Basse *et al.* [44] and Begg *et al.* [45] considered continuum size-structured models of the cell cycle where proliferation events alter the physical size of cells considered in the system. These particular studies have application to understanding cancer therapy and phytoplankton dynamics. Although these models did not consider spatial movement, they represent an approach to account for changes in cell size in a continuum model.

We also remark that our work is a first attempt to bridge a gap between different types of discrete models that are used to represent collective cell motion. For example, Cellular Potts Models (CPMs) represent biological cells exactly as they are observed in experiments by replicating the pixels that cells occupy in certain experimental images [46]. The changes in shape, position, and orientation of cells in the CPM are described with the same precision as in experimental movies. The CPM typically represents an individual biological cell as an agent on a lattice, and that particular agent might occupy more than one lattice site [46]. Therefore the CPM is very different from a traditional exclusion process model where each biological cell is represented as an agent that occupies a single lattice site [22,26–28]. From this point of view, the work

in the current manuscript begins to address questions about the relationship between the CPM and exclusion process models of cell motility. By generalizing the exclusion process model to allow each agent to occupy multiple lattice sites, we are making the generalized exclusion process model more like a CPM relative to traditional exclusion process models.

Two recent studies have attempted to identify a continuum description of the CPM by relating CPM results to the solution of a PDE model. Turner and coworkers [47] related their CPM results to a linear diffusion equation, while Lushnikov and coworkers [48] related their CPM results to a nonlinear diffusion equation. Both these previous works demonstrated a good match between the CPM results and the solution of the corresponding PDE model. In our work we have extended a traditional exclusion process model to account for variable agent aspect ratio and have analyzed the relevant continuum limit of this discrete model. Our generalized exclusion process model is more like the CPM relative to traditional exclusion process models, as previously outlined; however, much work remains to be done to obtain and complete understanding of the relationship between exclusion process models and the CPM. For example, our work does not include dynamic changes in cell shape or cell size during the simulations. These effects are routinely incorporated into the CPM.

The models presented in this work can be extended to consider other applications. For example, here we consider the case where agents are elongated and rod shaped so that each agent occupies L adjacent lattice sites on a square lattice where the dimension of the agent, relative to the lattice spacing, is $(L \times 1)$. It is also possible to consider larger square agents that occupy L^2 lattice sites so that the dimension of the agent, relative to the lattice spacing, is $(L \times L)$. For these larger square agents there is no need to consider any rotation events on a square lattice because these agents are rotationally symmetric with respect to the lattice. Following the same conservation arguments for these larger square agents, we arrive at an isotropic PME with $D_x(C) = D_y(C) = L^2[C(1-C)]^{(L-1)}$. Further extensions will be investigated in future work.

ACKNOWLEDGMENTS

We thank Professor Sean McElwain and Dr. Mike Plank for their helpful comments on a draft form of this manuscript. We also thank the thoughtful comments from two anonymous referees. S.W.M acknowledges support from the Australian Research Council through the Discovery Project DP0878011. R.E.B acknowledges support from Research Councils UK and St Hugh's College, Oxford.

[1] P. K. Maini, D. L. S. McElwain, and D. I. Leavesley, Tissue Eng. **10**, 475 (2004).
[2] P. K. Maini, D. L. S. McElwain, and D. Leavesley, Appl. Math. Lett. **17**, 575 (2004).
[3] J. A. Sherratt and J. D. Murray, Proc. R. Soc. London B **241**, 29 (1990).
[4] H. Sheardown and Y. L. Cheng, Chem. Eng. Sci. **51**, 4517 (1996).
[5] B. G. Sengers, C. P. Please, and R. O. C. Oreffo, J. R. Soc. Interface **4**, 1107 (2007).
[6] M. J. Simpson, D. C. Zhang, M. Mariani, K. A. Landman, and D. F. Newgreen, Dev. Biol. **302**, 553 (2007).
[7] J. A. Sherratt and B. P. Marchant, Appl. Math. Lett. **9**, 33 (1996).
[8] J. L. Vázquez, *The Porous Medium Equation* (Oxford Science Publications, Oxford, 2007).
[9] G. I. Barenblatt, *Scaling, Self-similarity, and Intermediate Asymptotics* (Cambridge University Press, Cambridge, 1996).
[10] T. P. Witelski, J. Math. Biol. **35**, 695 (1997).
[11] W. S. C. Gurney and R. M. Nisbet, J. Theor. Biol. **52**, 441 (1975).
[12] W. S. C. Gurney and R. M. Nisbet, J. Theor. Biol. **56**, 249 (1976).
[13] E. A. Carl, Ecology **52**, 595 (1971).
[14] J. D. Murray, *Mathematical Biology I: An Introduction*, 3rd ed. (Springer, Heidelberg, 2002).
[15] F. Sánchez Garduño and P. K. Maini, Appl. Math. Lett. **7**, 47 (1994).
[16] F. Sánchez Garduño and P. K. Maini, J. Diff. Eq. **117**, 281 (1995).
[17] T. P. Witelski, Appl. Math. Lett. **8**, 57 (1995).
[18] S. Harris, J. Phys. A: Math. Gen. **37**, 6267 (2004).
[19] R. A. Gatenby and E. T. Gawlinski, Cancer Res. **56**, 5745 (1996).
[20] M. J. Simpson, K. A. Landman, B. D. Hughes, and D. F. Newgreen, J. Theor. Biol. **243**, 343 (2006).
[21] M. J. Simpson, A. Merrifield, K. A. Landman, and B. D. Hughes, Phys. Rev. E **76**, 021918 (2007).
[22] M. J. Simpson, K. A. Landman, and B. D. Hughes, Physica A **388**, 399 (2009).
[23] M. J. Simpson, K. A. Landman, B. D. Hughes, and A. E. Fernando, Physica A **389**, 1412 (2010).
[24] M. J. Simpson, K. A. Landman, and B. D. Hughes, Physica A **389**, 3779 (2010).
[25] C. Deroulers, M. Aubert, M. Badoual, and B. Grammaticos, Phys. Rev. E **79**, 031917 (2009).
[26] E. Khain, L. M. Sander, and C. M. Schneider Mizell, J. Stat. Phys. **128**, 209 (2007).
[27] E. Khain and L. M. Sander, Phys. Rev. E **77**, 051129 (2008).
[28] E. Khain, C. M. Schneider Mizell, M. O. Nowicki, E. A. Chiocca, S. E. Lawler, and L. M. Sander, Europhys. Lett. **88**, 28006 (2009).
[29] T. M. Liggett, *Stochastic Interacting Systems: Contact, Voter and Exclusion Processes* (Springer, Berlin, 1999).
[30] D. Chowdhury, A. Schadschneider, and K. Nishinari, Phys. Life Rev. **2**, 318 (2005).
[31] J. Crank, *The Mathematics of Diffusion*, 2nd ed. (Oxford University Press, Oxford, 1975).
[32] E. A. Codling, M. J. Plank, and S. Benhamou, J. R. Soc. Interface **5**, 813 (2008).
[33] B. D. Hughes, *Random Walks and Random Environments*, Vol. 1 (Oxford University Press, Oxford, 1995).
[34] M. J. Simpson, C. Towne, D. L. S. McElwain, Z. Upton, Phys. Rev. E **82**, 041901 (2010).
[35] C. Zheng and G. D. Bennett, *Applied Contaminant Transport Modelling*, 2nd ed. (John Wiley, New York, 2002).

[36] T. Callaghan, E. Khain, L. M. Sander, and R. M. Ziff, J. Stat. Phys. **122**, 909 (2006).
[37] R. E. Baker and M. J. Simpson, Phys. Rev. E **82**, 041905 (2010).
[38] E. S. Oran and J. P. Boris, *Numerical Simulation of Reactive Flow*, 2nd ed. (Cambridge Universtiy Press, Cambridge, 2001).
[39] M. J. Simpson, K. A. Landman, and T. P. Clement, Math. Comput. Simul. **70**, 44 (2005).
[40] J. Donea and A. Huerta, *Finite Element Methods for Flow Problems* (John Wiley and Sons, West Sussex, 2003).
[41] D. T. Gillespie, J. Phys. Chem. **81**, 2340 (1977).
[42] J. A. Fozard, H. M. Byrne, O. E. Jensen, and J. R. King, Math. Med. Biol. **27**, 39 (2010).
[43] P. J. Murray, C. M. Edwards, M. J. Tindall, and P. K. Maini, Phys. Rev. E **80**, 031912 (2009).
[44] A. Basse, B. C. Baguley, E. S. Marshall, G. C. Wake, and D. J. N. Wall, Prog. Biophys. Mol. Bio. **85**, 353 (2004).
[45] R. Begg, D. J. N. Wall, and G. C. Wake, Math. Med. Biol. **22**, 371 (2005).
[46] F. Graner and J. A. Glazier, Phys. Rev. Lett. **69**, 2013 (1992).
[47] S. Turner, J. A. Sherratt, K. J. Painter, and N. J. Savill, Phys. Rev. E **69**, 021910 (2004).
[48] P. M. Lushnikov, N. Chen, and M. Alber, Phys. Rev. E **78**, 061904 (2008).